UNIVERSIDAD COMPLUTENSE DE MADRID

FACULTAD DE CIENCIAS FÍSICAS

Máster en Astrofísica

TRABAJO DE FIN DE MÁSTER

Trazadores de líneas de emisión especialmente relevantes en espectros ópticos de galaxias enanas con formación estelar

Tracers for emission lines especially relevant in optical spectra of star-forming galaxies

Laura Medina Crespo

Supervisado por:

Jesús Gallego Maestro

Curso académico 2025-26

UNIVERSIDAD COMPLUTENSE MADRID

Declaración responsable sobre autoría y uso ético de herramientras de Inteligencia Artificial (IA)

Yo, Laura Medina Crespo

con DNI/NIE/PASAPORTE: 77370021E

declaro de manera responsable que el/la presente (seleccionar opción):

- [ ] Trabajo Fin de Grado (TFG)
- [x] Trabajo Fin de Máster (TFM)
- [ ] Tesis Doctoral

titulado/a

Trazadores de líneas de emisión especialmente relevantes en espectros ópticos de galaxias enanas con formación estelar

Tracers for emission lines especially relevant in optical spectra of star-forming dwarf galaxies

es el resultado de mi trabajo intelectual personal y creativo, y ha sido elaborado de acuerdo con los principios éticos y las normas de integridad vigentes en la comunidad académica y, más específicamente, en la Universidad Complutense de Madrid.

Soy, pues, la persona autora del material aquí incluido y, cuando no ha sido así y he tomado el material de otra fuente, lo he citado o bien he declarado su procedencia de forma clara —incluidas, en su caso, herramientas de inteligencia artificial—. Las ideas y aportaciones principales incluidas en este trabajo, y que acreditan la adquisición de competencias, son mías y no proceden de otras fuentes o han sido reescritas usando material de otras fuentes.

Asimismo, aseguro que los datos y recursos utilizados son legítimos, verificables y han sido obtenidos de fuentes confiables y autorizadas. Además, he tomado medidas para garantizar la confidencialidad y privacidad de los datos utilizados, evitando cualquier tipo de sesgo o discriminación injusta en el tratamiento de la información.

En Madrid, a 31/05/2026

FIRMA

Firmado por MEDINA CRESPO LAURA - ***7002** el día 10/05/2026 con un certificado emitido por AC FNMT Usuarios

Abstract

We present a statistical analysis of the physical properties of dwarf star-forming galaxies in the low redshift universe ($z < 0.24$), based on a sample of 24 384 objects from the Sloan Digital Sky Survey (SDSS DR8) selected by absolute magnitude ($M_B > -18$), of which 1 473 show a significant detection ($S/N > 3$) of the auroral line [OIII]λ4363, used for the direct-method metallicities. We characterise the physical differences between emitters and non-emitters, finding the former are systematically lower in stellar mass, bluer, more compact, and more intensely star-forming. Using four complementary correlation statistics, we identify $D_{4000,N}$, $EW_0(\mathrm{H}\beta)$, and $\log EW_0([\mathrm{NeIII}]\,\lambda3869)$ as the strongest observational predictors of $\log EW_0([\mathrm{OIII}]\,\lambda4363)$, all accessible from low-resolution spectroscopy across a broad redshift range. Bayesian linear regressions reveal the emitter population splits into two ionisation regimes, consistent with the bursty nature of star formation in low-mass galaxies. The hardness of the ionising radiation field is further explored through the HeIIλ4686 line. Finally, we use the MOSAIC (ELT) exposure time calculator to argue that the selection criteria derived here are essential for efficient telescope time use in future programmes targeting direct-method metallicities at intermediate redshifts.

Resumen

Presentamos un análisis estadístico de las propiedades físicas de galaxias enanas con formación estelar en el universo a bajo redshift ($z < 0.24$), basado en una muestra de 24 384 objetos del Sloan Digital Sky Survey (SDSS DR8) seleccionada por magnitud absoluta ($M_B > -18$), de los cuales 1 473 tienen una detección significativa ($S/N > 3$) de la línea auroral [OIII]λ4363, usada para medir metalicidades por método directo. Caracterizamos las diferencias físicas entre emisoras y no emisoras, encontrando que las primeras tienen masas sistemáticamente menores, son más azules, compactas y con formación estelar más intensa. Con cuatro métodos estadísticos complementarios identificamos $D_{4000,N}$, $EW_0(\mathrm{H}\beta)$ y $\log EW_0([\mathrm{NeIII}]\,\lambda3869)$ como los predictores observacionales más potentes, todos accesibles con espectroscopía de baja resolución a cualquier redshift. Las regresiones bayesianas revelan que la población emisora se divide en dos regímenes de ionización, consistente con la naturaleza intermitente de la formación estelar en galaxias de baja masa. La dureza del campo de radiación ionizante se explora adicionalmente mediante la línea HeIIλ4686. Finalmente, usamos el calculador de tiempo de exposición de MOSAIC (ELT) para mostrar que los criterios de selección derivados son esenciales para un uso eficiente del tiempo de telescopio en futuros programas que busquen medir metalicidades por el método directo a desplazamientos al rojo intermedios.

Contents

1 Introduction **2**

1.1 The role of dwarf star-forming galaxies 2

1.2 Goal 3

2 Data and Sample Selection **3**

2.1 Data Sources 3

2.2 Pre-processing and Quality Criteria 5

2.3 Corrections and Derivation of Absolute Magnitudes 5
2.4 Sample Refinement 6
2.5 Final Sample Definition of [OIII]λ4363 emitters 8

3 The physical characterisation of [OIII]λ4363 emitters 9
3.1 Comparative Physical Properties 9
3.2 Star-Forming Main Sequence (SFMS) 12
3.3 Spectroscopic Classification: BPT Diagram 13
3.4 Correlation Analysis of Observables 14

4 Figure of merit for [OIII]λ4363 emitters 15
4.1 Two Populations: High and Low Ionisation 16
4.2 Quantifying the Relations: Bayesian Regressions 17

5 The case of HeIIλ4686 20

6 λ4363 emitters at different redshifts: A scientific case for the MOSAIC instrument at ELT 22

7 Summary and Conclusions 23

8 References 25

1 Introduction

1.1 The role of dwarf star-forming galaxies

The mechanism governing galaxy evolution is star formation. When a star is born, and it evolves and dies, it generates a series of changes, both in its surroundings and within itself, that shape the chemical and dynamical evolution of its host galaxy. This star formation is a hierarchical process that happens on a huge scale, from gas accretion onto galactic discs down to the final assembly of individual stars and clusters, passing through the formation of cold neutral gas and molecular clouds (Kennicutt et al. 2012).

The star formation history of a galaxy is written in the evolution of the SFR, and leaves its mark on the galaxy's spectrum through emission lines, which are therefore powerful diagnostic tools for understanding physical conditions within galaxies. Properties such as electron temperature, metallicity and ionisation parameter all leave their imprint on the processes responsible for the spectral lines (Kewley et al. 2019). Among these are the 'auroral lines': forbidden emission lines triggered by particle collisions in ionized interstellar gas, carrying higher energy than standard nebular lines (Laseter et al. 2024). In practice, ratios of specific lines from the same ion are particularly sensitive to electron temperature. [N II] λ5756/[N II] λ6584, [S II] λ4969/[S II] $\lambda\lambda$6717, 6731 and [O III] λ4363/[O III] λ5007 are among the most used. Combining these with a hydrogen recombination line (such as Hβ) yields ratios depending only on temperature and ionic abundance, enabling the inference of ionic abundances via the direct method (Brazzini et al. 2024).

The [OIII]λ4363 line is the most desirable of these for its proximity to other optical emission lines (Laseter et al. 2024). Its intensity is determined by the collision rate between O^{++} ions and electrons, which depends on n_e and fundamentally on T_e. At low electron temperatures, typical of metal-rich regions, very few electrons carry enough energy to excite the high-energy levels responsible for [OIII]λ4363, making this line intrinsically faint, anywhere from 10 to 100 times weaker than neighbouring oxygen and Balmer lines. As temperature rises, however, the population of energetic electrons grows exponentially, making $F(\lambda4363)/F(\lambda\lambda4959, 5007)$ extremely sensitive to changes in T_e of the O^{++} zone (Sanders et al. 2016). The method relies on a simple five-level photoionisation model of a single atom, assuming a homogeneous medium to compute T_e (Osterbrock et al. 2006), from which ionic abundances are derived. Furthermore, the physical basis of the direct method is redshift-invariant: locally calibrated strong-line relations and excitation diagrams are consistent from $z \sim 0$ to at least 3.1 (Gburek et al. 2019).

The importance of star-forming dwarf galaxies stems from the great revelation of JWST spectroscopic observations, summarised by Atek et al. (2024): 'Most of the photons that reionised the universe come from dwarf galaxies'. This is reinforced by recent JWST studies of compact, low-mass galaxies with high sSFRs and extreme emission lines spanning $4 \lesssim z \lesssim 10$, finding that ξ_{ion} correlates with the high-ionization, low-metallicity conditions characteristic of these systems (Llerena, M. et al. 2026). In the local universe, galaxies where [OIII]λ4363 is detected tend to be less metal-rich, less luminous and more highly ionised than those where it is not (Hoyos et al. 2006). With this in mind, we seek a representative sample of star-forming dwarf galaxies with and without [OIII]λ4363 detections, aiming to find indirect low-redshift indicators that can be extrapolated to high redshift for a deeper understanding of these systems.

1.2 Goal

The objective of this study is to explore the physical properties of star-forming dwarf galaxies in the low-redshift universe through its emission lines, with particular attention to the auroral line [OIII]λ4363. These tracers allow us to estimate interstellar medium metal abundances, as well as other physical parameters such as the ionisation parameter and the electron temperature. Together, these indicators will serve to guide the design of future studies on galaxy samples at different redshifts.

To this end, I have used the Sloan Digital Sky Survey (SDSS) database to compile a significant sample on which to carry out the analysis, which will be optimised to resemble the properties of high-redshift galaxies. The goal is to explore possible correlations between the presence and strength of emission lines with both the environment and other physical parameters that are straightforward to measure for large galaxy samples at different redshifts.

2 Data and Sample Selection

2.1 Data Sources

For this study, we used spectroscopic and photometric data from the Sloan Digital Sky Survey (SDSS), specifically from Data Release 8 (DR8) (Aihara et al. 2011). This release was chosen because it contains the Legacy Survey data, a reprocessed and recalibrated compilation of all photometric and spectroscopic observations carried out in the stages before the SDSS-III. The initial sample was constructed by cross-matching two main sources.

For the derivation of the physical properties of the sample, we employed the value added

catalogues (VACs) developed by the Max Planck Institute for Astrophysics and Johns Hopkins University (MPA-JHU) group (SDSS-III Collaboration 2012). This dataset improves upon the emission-line flux measurements of the official SDSS's pipeline through a careful subtraction of the underlying stellar continuum using stellar population models (Bruzual et al. 2003). We also made use of stellar mass estimates (M_*) (Kauffmann et al. 2003) and star formation rates (SFR) (Brinchmann et al. 2004) provided by this catalogue, both of which include aperture corrections to recover the global properties of galaxies outside the spectroscopic fibre, along with gas-phase metallicity estimated through photoionisation models for star-forming galaxies (Tremonti et al. 2004).

The FITS files of this catalogue (`galSpecInfo`, `galSpecLine`, `galSpecExtra` and `galSpecIndx`) providing these derived spectral measurements were downloaded.

To complement the spectral analysis from the MPA-JHU catalogue, photometric information was gathered through queries to the SDSS CasJobs database. The spectral sample was cross-matched with the SDSS primary photometric catalogue (PhotoObj) using the unique identifier SpecObjID, keeping only the objects flagged as reliable (RELIABLE=1). Three sets of key parameters were extracted for each galaxy:

1. (1) Photometry (ugriz): model magnitudes (modelMag), and fibre magnitudes (fiberMag), more importantly used to characterise the sample of dwarf galaxies by their magnitude.
2. (2) Structural parameters: Petrosian radii, to characterise the physical size and concentration of the galaxies.
3. (3) Galactic extinction: extinction values for each filter were extracted based on the Schlegel et al. (1998) (SFD) dust maps, enabling correction for Galactic reddening as described in the methodology of Brinchmann et al. (2004) and Kauffmann et al. (2003).

The merging of these tables was carried out using the unique identifier `SPECOBJID`. An initial cleaning of null or corrupted identifiers was applied, along a redshift filter $z > 0.001$ to avoid the inclusion of stars from our own Galaxy or instrumental measurement errors that could bias the results. This yielded an initial sample of 718 719 galaxies.

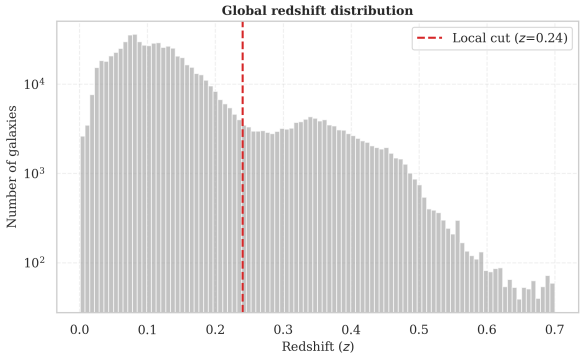

Figure 1: Redshift distribution of the initial galaxy sample.

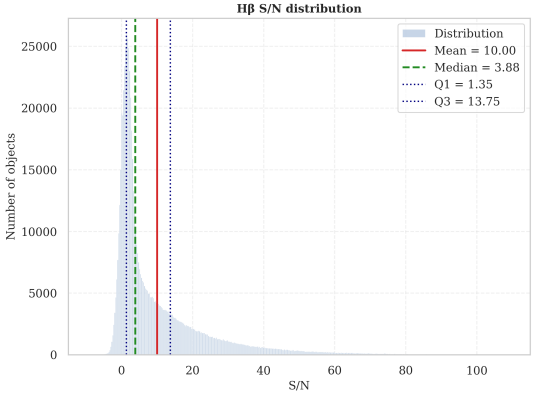

Figure 2: Distribution of SNR of Hβ.

Some observational features of this initial selection are illustrated in Figures 1 and 2. As can be seen, the sample spans a broad redshift range up to $z \sim 0.7$, though the bulk of galaxies are concentrated below $z \sim 0.24$, while the Hβ signal-to-noise ratio distribution exhibits a prominent peak at $S/N \sim 1.4$ before decreasing towards higher values.

2.2 Pre-processing and Quality Criteria

For this analysis, the procedure begins with the definition of a cosmological framework, where we use a flat Lambda Cold Dark Matter (ΛCDM) universe model. Consensus values for the Hubble constant and matter density parameters are adopted.

Quality masks based on the SDSS reliability indicators were then applied, keeping only spectra classified as reliable (`RELIABLE == 1`) by the MPA-JHU pipeline and with a confirmed redshift measurement free of technical warnings (`Z_WARNING == 0`).

A redshift filter $z < 0.6$ is added to allow the later application of K-correction formulae (Chilingarian et al. 2010). Since we are targeting a local sample, this cut has no practical effect. To ensure the reliability of the K-corrections and the baseline photometry both, a quality filter on the apparent magnitudes from the SDSS catalogue was applied.

The sample was restricted to galaxies with observed magnitudes in the range $12 <$ modelMag < 23 in the g and r bands. The faint limit ($m < 23$) was set in accordance with the 95% photometric completeness limit of the SDSS ($r \approx 22.2$, (Abazajian et al. 2004)), beyond which photometric errors become large and the $g - r$ colours introduced into the K-correction polynomials lose physical meaning. The bright limit ($m > 12$), on the other hand, serves to exclude spatially very extended objects or those that saturate the telescope's CCD sensors, which compromises magnitude estimation (Lupton et al. 2001; Strauss et al. 2002). Finally, a filtering of unphysical $g - r$ colour values was performed to remove galaxies contaminated by nearby stars.

2.3 Corrections and Derivation of Absolute Magnitudes

In order to facilitate the comparison of our results with the classical literature, which predominantly uses the Johnson-Cousins filter system (B, V), we transformed the absolute magnitudes derived in the native SDSS system (u, g, r, i, z) into this system, before applying a cut in B to delimit our sample of dwarfs.

Observed magnitudes are subject to distortions caused both by the interstellar medium of the Milky Way and by the expansion of the universe. To address the first effect, Galactic extinction corrections were applied using the dust maps of Schlegel et al. (1998), which analytically subtract the absorption in each photometric filter as a function of the object's position on the celestial sphere.

After that, we turned to the problem of the K-correction. Since galaxies recede from us, their spectra are redshifted, meaning that a fixed filter observes a different part of the rest-frame emission depending on redshift. To correct for this bias, the analytical approximations proposed by Chilingarian et al. (2010) were employed. We used the original code of this author (available at `http://kcor.sai.msu.ru/`), with slight modifications so we could estimate the uncertainty and therefore, propagate the errors through this entire process.

To determine how intrinsically bright a galaxy is, we need to know its distance. We use the luminosity distance (D_L) in Mpc, computed from the redshift (z). From D_L, the distance modulus (DM) is calculated with: $DM = 5\log_{10}(D_L[\mathrm{pc}]) - 5 = 5\log_{10}(D_L[\mathrm{Mpc}]) + 25$ and absolute magnitudes were then obtained by applying: $M = m - DM - K(z)$.

To then transform the absolute magnitudes in the SDSS system (u, g, r, i, z) into the Johnson-Cousins system, we applied the transformation equations computed by (Lupton 2005). These relations allow the derivation of M_B and M_V from the g band and the intrinsic colour ($g - r$)

through the following expressions:

$$M_B = M_g + 0.3130(M_g - M_r) + 0.2271 \qquad (1)$$

$$M_V = M_g - 0.5784(M_g - M_r) - 0.0038 \qquad (2)$$

To add statistical robustness to the analysis, we also implemented the empirical transformations of (Cook et al. 2014), which were calibrated specifically for nearby galaxy populations and involve a broader spectral coverage by integrating the u and i bands:

$$M_B = 1.27M_g - 0.27M_i + 0.16 \qquad (3)$$

$$M_V = 0.18M_u + 0.82M_r - 0.02 \qquad (4)$$

A critical aspect of this step is the change of flux reference system. While the original SDSS magnitudes are defined in the AB system, the calibration constants of both Lupton (2005) and Cook et al. (2014) incorporate the conversion term necessary for the resulting magnitudes to be directly calibrated in the Vega system.

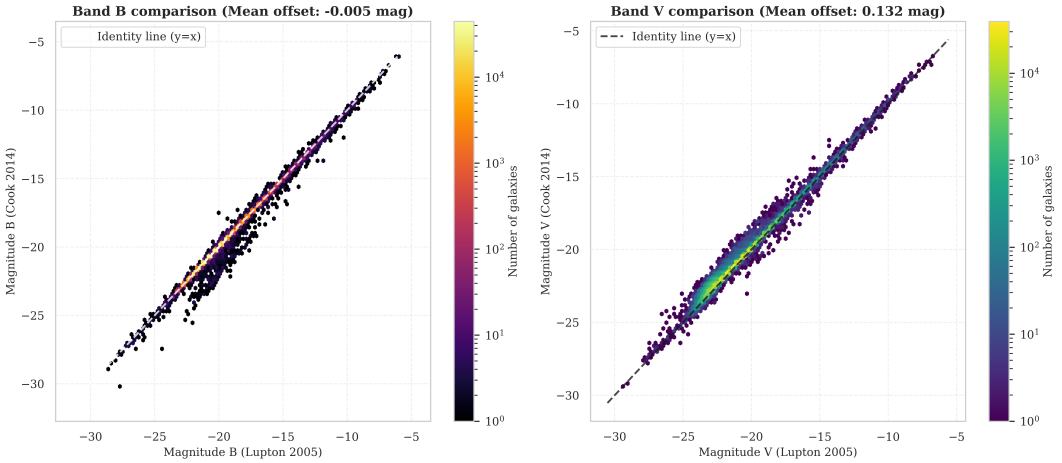

Figure 3: Comparison of absolute magnitude values obtained with the different photometric transformations.

As can be seen in Figure 3, the mean offset between the two transformations is quite small. In the B band the mean offset is of only -0.005 mag, with mean uncertainties are of 0.028 mag (Lupton) and 0.050 mag (Cook). In the V band the offset is larger, 0.1 mag, but since the dwarf galaxy selection is defined exclusively in B, this has no impact on the sample. Given that the Lupton transformations produce smaller errors in both bands they were adopted for the remainder of the analysis.

2.4 Sample Refinement

The Hβ emission line plays a central role in this analysis: it is required for BPT classification (Baldwin et al. 1981), for the derivation of star formation rates, and as the reference line for reddening corrections. A reliable detection of Hβ is therefore essential for the characterisation of any galaxy in the sample. To assess how the choice of detection threshold affects the sample composition, two sub-samples were defined: a broad one ($S/N_{\mathrm{H}\beta} > 3$, $N = 398{,}345$) and a strict one ($S/N_{\mathrm{H}\beta} > 5$, $N = 322{,}035$), the latter retaining 80.8% of the former (see the overall distribution in

Figure 2). The choice between them was made on the basis of the statistical tests described below, balancing the gain in measurement reliability against the risk of introducing systematic biases into the sample composition.

Quantifying the representativity of the sub-sample

The k-sample Anderson-Darling test (Anderson et al. 1952) was applied, which measures the cumulative discrepancy between empirical distributions with greater sensitivity in the tails than the classical Kolmogorov-Smirnov test. High-quality galaxies ($S/N > 5$) were compared against those that would be excluded when raising the threshold ($3 < S/N \leq 5$), using the logarithmic stellar mass ($\log M_\star/\mathrm{M}_\odot$, column `LGM_TOT_P50` of the MPA-JHU catalogue) as the control variable. The test rejected the null hypothesis of distributional identity, confirming that the objects lost by raising the threshold have systematically different mass properties and do not represent a random draw from the population.

In order to characterise in detail the nature of the bias introduced, a two-sample Kolmogorov-Smirnov (KS) test (Kolmogorov 1933; Smirnov 1948) was then applied to a broad set of physical and observational properties. The statistic D represents the maximum separation between the cumulative distribution functions (CDFs) of both samples, ranging from 0 to 1. Given the sample size ($\sim 3.5\times10^5$ objects), the p-value is systematically zero for any real difference, so the meaningful diagnostic is the effect size: $D < 0.05$ is considered negligible, $0.05 \leq D < 0.10$ moderate, and $D \geq 0.10$ notable. The results are summarised in Table 1.

Property	N $(S/N > 3)$	N $(S/N > 5)$	D	$\Delta\tilde{x}$
Stellar Mass $[\log M_\star]$	390 851	318 471	0.076	-0.106 dex
$\log$ SFR	375 988	307 479	0.083	$+0.106$ dex
Redshift z	398 345	322 035	0.035	-0.005
Colour $g-r$ (rest frame)	398 345	322 035	0.121	-0.039 mag
Absolute magnitude M_r	398 345	322 035	0.061	$+0.165$ mag
$D_{4000,N}$	398 345	322 035	0.132	-0.050
$\log L(\mathrm{H}\beta)$	398 345	322 035	0.046	$+0.067$ dex
$\mathrm{EW}_0(\mathrm{H}\beta)$	398 325	322 015	0.126	$+0.664$ Å
Metallicity	156 588	156 588	0.000	0.000

Table 1: Kolmogorov-Smirnov test results comparing the $S/N_{\mathrm{H}\beta} > 3$ and $S/N_{\mathrm{H}\beta} > 5$ samples. D is the maximum-distance statistic between CDFs; $\Delta\tilde{x}$ is the difference in medians (strict minus broad sample).

The results reveal that the $S/N_{\mathrm{H}\beta} > 5$ cut does introduce biases with respect to the baseline sample. However, the direction of these biases is consistent with the selection criteria adopted in this work. The strict sample favours objects of lower mass ($\Delta\overline{M}_\star \approx -0.11$ dex), bluer colour ($\Delta\overline{g-r} \approx -0.04$ mag), lower $D_{4000,N}$ index (index of the break at 4000 Å in its narrow definition by Balogh et al. (1999); is a tracer of the mean stellar age and star formation history) and higher star formation rate. These are precisely the characteristics of the star-forming dwarf galaxies that make up our target population. The completeness analysis shows that the retained fraction exceeds 85% for galaxies with $\log(M_\star/\mathrm{M}_\odot) < 10.5$ and $z < 0.15$, which is precisely the range of interest (see Fig. 4). The loss of objects is concentrated around massive, passive galaxies that would in any case also be excluded at the final selection cut. This is also reflected in the BPT classification given in the MPA-JHU catalogue, as the fraction of pure star-forming galaxies (class 1) rises from 40.3% to 49.9% under the stricter threshold.

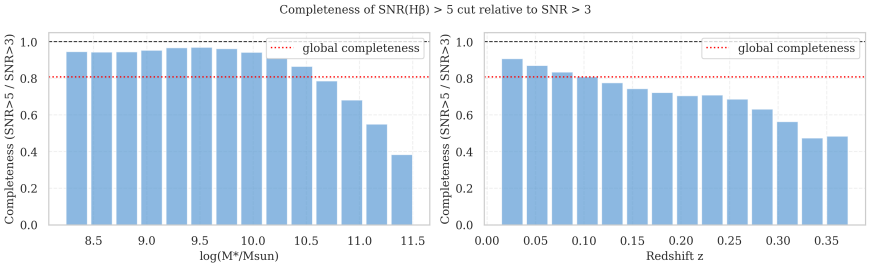

Figure 4: Completeness of the $S/N_{\mathrm{H}\beta} > 5$ cut relative to $S/N > 3$ as a function of stellar mass (left) and redshift (right). The dashed red line indicates the global completeness (80.9%).

In light of these results, the threshold $S/N_{\mathrm{H}\beta} > 5$ was adopted, prioritising the reliability of emission-line measurements over statistical volume.

To avoid evolutionary biases and distance-related selection effects (Malmquist bias), we then examined the redshift distribution of the sample. The catalogue contains objects up to $z \approx 0.6$, though after imposing the $S/N_{\mathrm{H}\beta} > 5$ requirement no galaxies remain above $z \approx 0.4$, a limit that defines the extended sample. Beyond $z > 0.24$, however, the K-corrections become less reliable and the $3''$ SDSS spectroscopic fibre subtends an increasing fraction of the galaxy's apparent angular size, introducing non-negligible aperture effects (Kewley et al. 2005).

To quantify this, the KS analysis was repeated comparing the extended sample ($z < 0.40$) against the nearer sample ($z < 0.24$) over the same set of physical properties. Including objects with $z > 0.24$ turns out to introduce a significant bias towards more massive galaxies: the statistic reaches $D = 0.20$ in stellar mass, with $\Delta\overline{M}_\star > 0.2$ dex, which can be explained by the loss of faint dwarf galaxies at greater distances. The completeness analysis confirms that the retained fraction drops below 70% for $z > 0.20$. The cut $z < 0.24$ was therefore adopted as the cosmological limit of the sample.

2.5 Final Sample Definition of [OIII]λ4363 emitters

Starting from the master catalogue of 312 474 galaxies, a physical pre-filtering was applied to the key emission lines. Specifically, we required positive, non-saturated fluxes for both Hβ and [OIII]λ5007. This step is physically motivated: Hβ can appear in absorption in passive galaxies, where the underlying stellar continuum fills in or reverses the emission feature, while [OIII]λ5007 is a forbidden line that can only exist in emission by nature, so a negative flux simply reflects a non-detection or instrumental noise rather than any physical signal. Imposing these constraints is therefore not an arbitrary cut but a way of ensuring that the lines we later analyse carry real physical information. After this filtering, the clean sample contains 311 147 galaxies, corresponding to 99.6% of the original catalogue.

Within this clean sample, 5 862 objects were identified with a significant detection of [OIII]λ4363 ($S/N > 3$). Dwarf galaxies were then defined by three absolute magnitude thresholds in the B band, and in each case the sample was split according to whether or not [OIII]λ4363 was detected.

The $M_B > -18$ limit was chosen, a threshold consistent with classical usage, where the dwarf regime is taken to extend to approximately $M_B \geq -18.5$ (Grebel 1998). This choice also increases sample completeness and preserves a larger, more statistically useful dataset for the following analysis. The sample with significant detection of [OIII]λ4363 will be called [OIII]λ4363 emitters.

Dwarf cut	Clean sample	Total dwarfs	With [OIII]λ4363	Without [OIII]λ4363
$M_B > -18$	311 147	24 384	1 473 (6.0%)	22 911 (94.0%)
$M_B > -16$	311 147	3 505	437 (12.5%)	3 068 (87.5%)
$M_B > -14$	311 147	982	104 (10.6%)	878 (89.4%)

Table 2: Composition of the dwarf galaxy sample according to the absolute magnitude M_B cut and the detection of [OIII]λ4363 ($S/N > 3$).

3 The physical characterisation of [OIII]λ4363 emitters

In this section, the results of the statistical and spectroscopic analysis performed on the sample of star-forming dwarf galaxies are presented, covering the comparative characterisation of both populations, their classification in the BPT diagram, the identification of observational predictors of $\log EW([\mathrm{O\,III}]\,\lambda4363)$, and the quantification of these relations through Bayesian regression.

3.1 Comparative Physical Properties

To explore the differences between dwarf galaxies [OIII]λ4363 emitters and non-emitters, the distributions of a set of key physical and observational properties are compared (Figures 5 and 6).

Starting with the observed properties, the optical colour $g - r$ (Fig. 5a) serves as an integrated indicator of the effective temperature of the dominant stellar population. Galaxies with [OIII]λ4363 show a median of $g - r = 0.20$ mag, noticeably bluer than dwarfs without detection ($g - r = 0.43$ mag). This difference is a consequence of the presence of newly formed O and B stars that dominate the UV and blue-optical emission. This bluer colour is in turn consistent with the lower $D_{4000,N}$ values observed in these galaxies (Fig. 5b), which measures the strength of the continuum break at 4000 Å and acts as a tracer of mean stellar age (Balogh et al. 1999; Kauffmann et al. 2003). In fact, galaxies with [OIII] emission show a median of $D_{4000,N} = 1.01$, a lower value than that of galaxies without detection (median of 1.21). This occurs because young stellar populations lack the old, cool K and M giant stars that produce the strong metal-line blanketing responsible for the 4000 Å break.

If we continue to the Hβ emission line, the result obtained directly supports the scenario of intense stellar activity. As seen in Fig. 5c, galaxies with [OIII]λ4363 emission show a significantly higher Hβ flux, with a median of $\log_{10} F = -14.50$ erg s^{-1} cm^{-2}, compared to the value of -15.45 for galaxies without detection. The intrinsic luminosity of this line (Fig. 6c) tells a similar story, as galaxies with [OIII] reach a median of $\log_{10} L = 39.30$ erg s^{-1}, while those without it sit at 38.79 erg s^{-1}. These high flux and luminosity values are the signature of intense and compact star-forming bursts, a fundamental physical condition that increases the visibility of faint auroral emission lines (Hoyos et al. 2006).

It is worth noting that the separation between the two populations is larger in flux (~ 0.95 dex) than in luminosity (~ 0.51 dex). This discrepancy is a direct manifestation of a selection effect tied to the Malmquist bias: because the [OIII]λ4363 auroral line is intrinsically faint, its detection requires high observed fluxes. For a given range of dwarf luminosities, the sample with [OIII] detection is therefore inevitably skewed towards objects at smaller distances, as is can be seen in the redshift comparison shown in Fig. 5c.

The rest-frame equivalent width of Hβ, EW_0(Hβ) (Fig. 5e), acts as an indicator of the age of the stellar burst and the hardness of the ionising radiation field (Brinchmann et al. 2004). Dwarfs with [OIII]λ4363 detection show a median of $EW_0(\mathrm{H}\beta) = 26.83$ Å, roughly an order of magnitude above

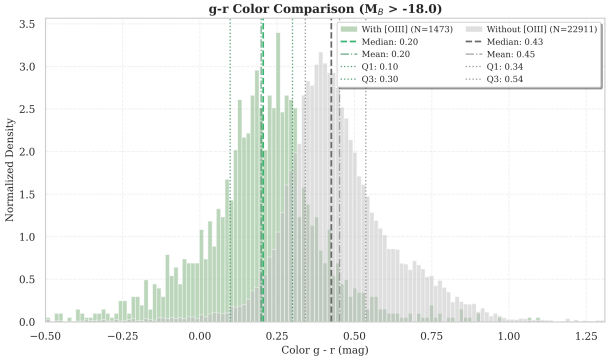

(a) $g - r$ colour

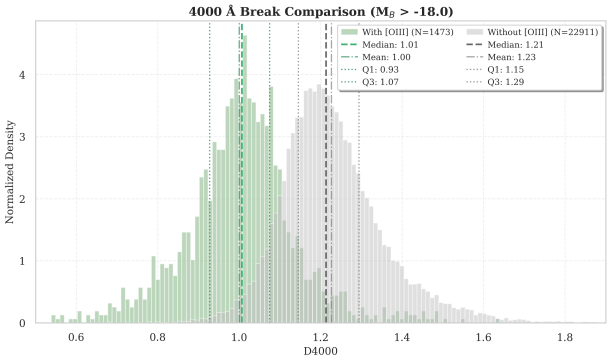

(b) Break at 4000 Å ($D_{4000,N}$)

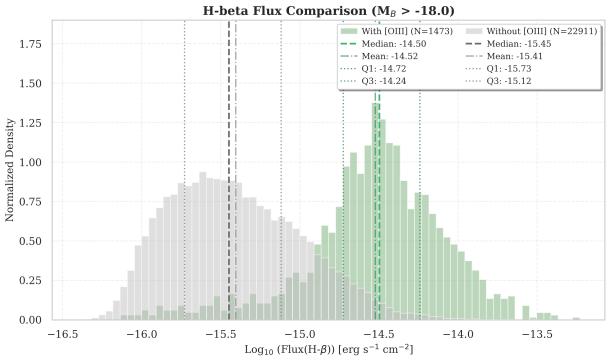

(c) Hβ flux

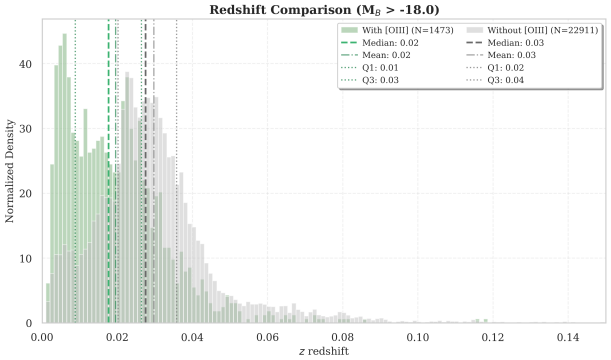

(d) Redshift

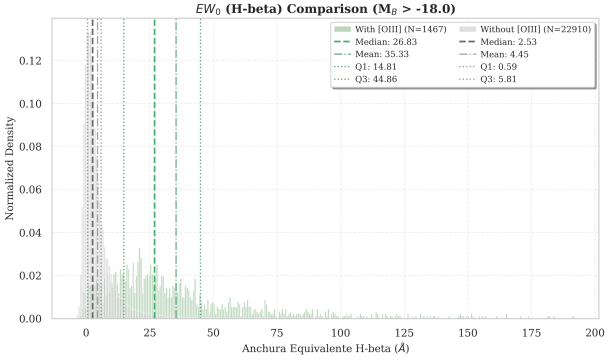

(e) Rest $EW(\mathrm{H}\beta)$

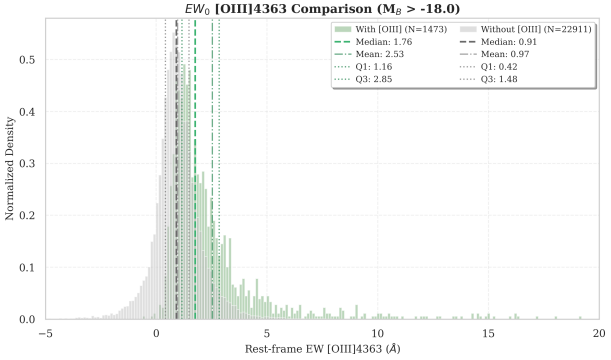

(f) Rest $EW([\mathrm{OIII}]\lambda 4363)$

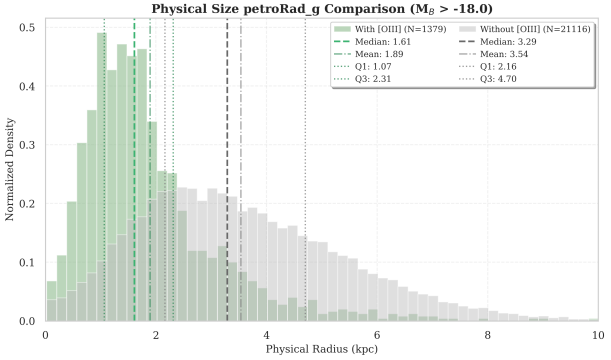

(g) g band radius

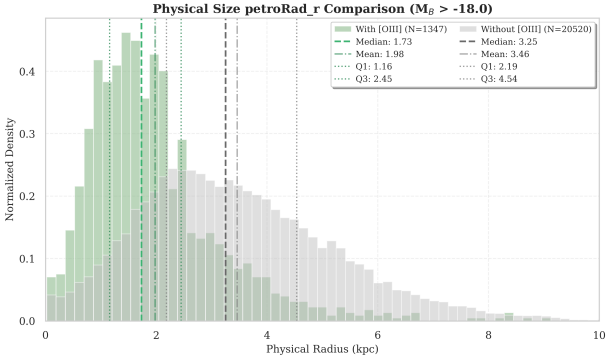

(h) r band radius

Figure 5: Comparison of observed properties for the dwarf emitters and non-emitters.

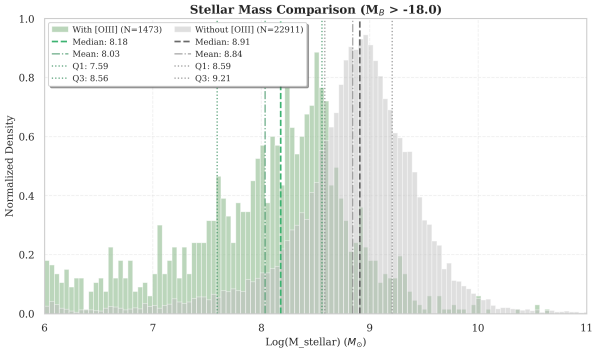

(a) Stellar mass, model derived property.

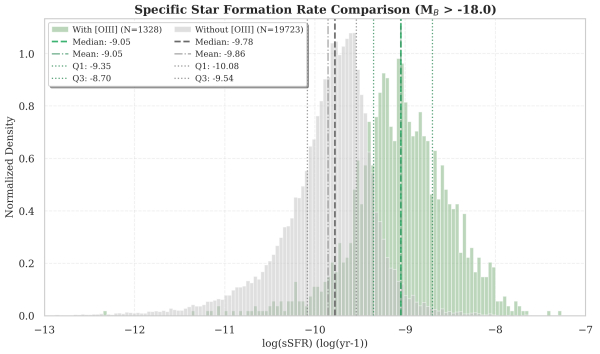

(b) sSFR, model derived property.

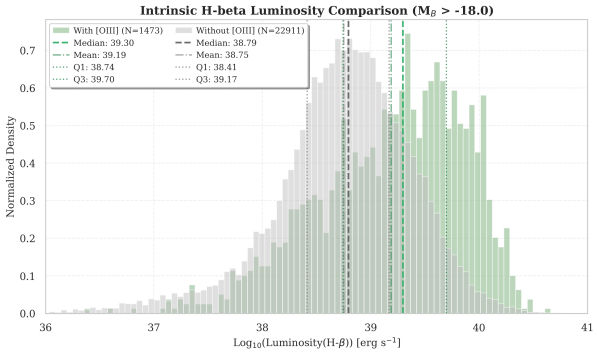

(c) Hβ luminosity, calculated from flux.

Figure 6: Comparison of physical properties.

that of non-emitters dwarfs (2.53 Å). This marked difference confirms that galaxies with the auroral line are made of much younger stellar populations. Physically, in the limit $EW_0(\mathrm{H}\beta) \to 0$, the stellar continuum from ageing populations dominates the spectrum and suppresses faint emission lines, which explains the close dependence between the visibility of the auroral line and the burst strength identified in previous analyses (Laseter et al. 2024).

Similarly, the distribution of $EW_0([\mathrm{OIII}]\lambda4363)$ (Fig. 5f) reveals the extreme nature of this subsample, with a median of 1.76 Å compared to 0.91 Å for galaxies where the line goes undetected. Systems in the high-value tail of this distribution show properties analogous to *Green Peas*: compact, high-excitation, low-metallicity galaxies regarded as the best local analogues of the sources that drive the reionisation of the early universe (Atek et al. 2024).

Regarding physical size, dwarfs with [OIII]λ4363 detection show a noticeably more compact morphology than the rest of the sample (Fig. 5g, h). Using the Petrosian radius converted to kiloparsecs, these galaxies show a median of 1.61 kpc in the g band and 1.73 kpc in the r band, values that contrast with those of galaxies without detection, whose median radii are 3.29 kpc and 3.25 kpc, respectively. This compactness is a characteristic feature of high-excitation systems (Sanders et al. 2016); in smaller volumes, the ionising photon density increases, raising the ionisation parameter and sustaining the high electron temperatures required for auroral line emission. Furthermore, this compact structure increases the galaxy's surface brightness, facilitating the detection of faint spectral features against the background noise.

Stellar mass ($\log M_\star/M_\odot$, Fig. 6a) acts as an indirect regulator of gas temperature through its connection to metallicity. Galaxies with [OIII]λ4363 detection show a median of $\log M_\star = 8.18$, compared to 8.91 for dwarfs without detection, a difference of 0.73 dex. Following the mass-

metallicity relation (Andrews et al. 2013), these lower masses imply a lower abundance of metals in the interstellar medium. Metal deficiency, in turn, weakens the main radiative cooling channels of the ionised gas, keeping the electron temperature (T_e) high enough to allow collisional excitation of the O^{2+} auroral line. This is a regime much harder to reach in more massive, metal-enriched systems, where efficient cooling suppresses the line before it can be observed.

The specific star formation rate ($\log \mathrm{sSFR}$, Fig. 6b) shows that line detection depends not only on mass but also on the intensity of the current star-forming episode. [OIII] emmiters show a median of $\log \mathrm{sSFR} = -9.05$, compared to -9.78 in the rest of the sample. This higher sSFR means that a significant fraction of the total stellar mass was formed very recently, ensuring an abundant population of short-lived massive stars that emit the high-energy photons necessary to overheat the gas and generate the high degree of ionisation observed in these systems (Kewley et al. 2019).

To complement the physical characterisation, it was analysed whether galaxies exhibiting the [OIII]λ4363 line possess a distinctive morphology. By cross-matching the sample with the visual classifications of Galaxy Zoo 2 (Willett et al. 2013), a clear divergence between the two populations is observed. While only about 22.6 to 29.2% of the galaxies are classified, dwarfs with the auroral line show an over-representation of irregular and elliptic morphologies compared to dwarfs without detection. The high fraction of objects classified as elliptical likely reflects extremely compact Green Pea-type systems appearing as barely resolved sources in SDSS images, misidentified as elliptical morphologies by non-expert classifiers (Cardamone et al. 2009).

To assess the statistical significance of this difference, a χ^2 homogeneity test was performed over the well-defined morphological categories, which yields $\chi^2 = 87.09$ with $p \ll 0.001$, leading to rejection of the null hypothesis that both populations share the same morphological distribution (Wall et al. 2012). Galaxies with [OIII]λ4363 are statistically biased towards irregular or compact systems, consistent with works associating extreme starburst episodes with morphological disturbances or gravitational interactions.

3.2 Star-Forming Main Sequence (SFMS)

The specific star formation rate ($\log \mathrm{sSFR}$) versus stellar mass ($\log M_\star$) diagram allows us to place these objects in the context of their galactic evolution and compare them with the star-forming main sequence. In Figure 7a, a clear segregation between both populations is observed.

While the general sample of dwarf galaxies without detection of the auroral line clusters around $\log M_\star \sim 8.9$ and $\log \mathrm{sSFR} \sim -9.78$, the group with [OIII]$\lambda$4363 shifts towards significantly lower masses ($\log M_\star \sim 8.1$) and more intense star formation activity ($\log \mathrm{sSFR} \sim -9.05$). This separation is not coincidental, and it connects naturally to what the recent literature tells us about these systems.

At the low mass end, the main sequence is noisier and the scatter increases considerably. As proposed by Andrews et al. (2013), in this regime ($M_\star \lesssim 10^9\, M_\odot$), the gravitational potential wells are shallow enough that metals are more easily expelled, keeping the gas metallicity low and the electron temperature high enough to excite the [OIII]λ4363 line.

At the same time, the high sSFR of the [OIII] emitters indicates to an episodic mode of star formation rather than a continuous one. As discussed by Atek et al. (2022), low-mass galaxies tend to form stars through violent, short-lived bursts, and it is precisely during these activity peaks that the ionising flux reaches the levels needed for the auroral line to emerge above the stellar continuum. This explains why galaxies with [OIII]λ4363 detections are systematically above the mean of the general population in this diagram.

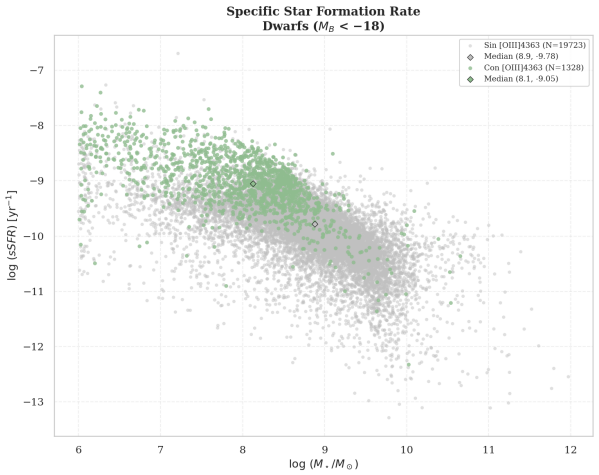

(a) Relation between sSFR and stellar mass for the dwarf sample ($M_B > -18$). Diamonds indicate the medians: $(\log M_\star, \log \mathrm{sSFR}) = (8.1, -9.05)$ for the [OIII] sample (green) and $(8.9, -9.78)$ for the sample without detection (grey).

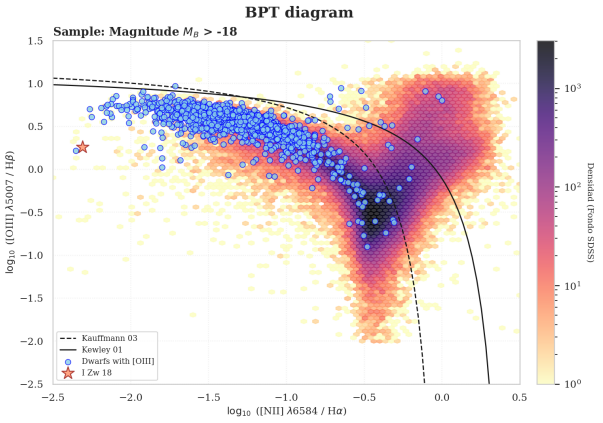

(b) BPT diagram. The hexagonal density map represents the distribution of the clean SDSS catalogue. The blue points correspond to dwarfs with [OIII]λ4363 detection ($S/N > 3$). Demarcation lines from (Kauffmann et al. 2003) (dashed) and (Kewley et al. 2001) (solid) are shown.

Figure 7: Analysis of the dwarf galaxy sample ($M_B > -18$).

3.3 Spectroscopic Classification: BPT Diagram

The BPT diagnostic diagram (Baldwin et al. 1981), which plots the emission-line ratios $\log([\mathrm{OIII}]\lambda5007/\mathrm{H}\beta)$ against $\log([\mathrm{NII}]\lambda6584/\mathrm{H}\alpha)$, provides a way to classify the dominant ionisation source of the nebular gas. Figure 7b shows this distribution for the dwarf galaxy sample ($M_B > -18.0$), overlaid on the density map of the clean SDSS sample (of 311 147 galaxies).

The vast majority of dwarfs with [OIII]λ4363 detection (blue points) fall in the pure star-forming region, delimited by the Kauffmann et al. (2003) curve, and are concentrated towards the upper-left extreme of the sequence. This region, characterised by low [NII]/Hα ratios and high [OIII]/Hβ excitation, is the domain of low-metallicity, high ionisation-parameter systems, properties consistent with those of local analogues of high-redshift galaxies recently detected by JWST (Laseter et al. 2024).

A subset of the sample falls in the transition region between the Kauffmann et al. (2003) and Kewley et al. (2001) curves. In low-metallicity systems with high excitation, however, this displacement does not necessarily point to the presence of an active nucleus. As discussed by Kewley et al. (2019) and Mazzolari et al. (2024), unusually hard ionising radiation fields in young stellar clusters can produce line ratios that are similar to AGNs, particularly in extreme low-metallicity and high ionisation environments.

One object stands out at the lower-left extreme of the distribution, marking the lowest metallicity and highest ionisation in the sample. Its position coincides with that of I Zw 18 (marked with an orange star), the galaxy with the lowest known oxygen abundance in the local universe (Kehrig et al. 2016). The fact that our sub-sample traces this low-metallicity branch lends confidence to the selection procedure and suggests we are looking at a group of galaxies in an early and active evolutionary state.

Taken together, the extreme position of these galaxies in the BPT diagram is consistent with their compact and low-mass nature. Small physical sizes and high specific star formation rates raise

the ionising photon density and elevate the ionisation parameter, pushing these systems towards the high-excitation end of the star-forming sequence.

3.4 Correlation Analysis of Observables

After classifying the sample using the BPT diagram, the next step is to identify which physical properties or spectral indicators show a statistical connection with the intensity of the [OIII]λ4363 line. This analysis constitutes the necessary prior step to determining which variables are the best candidates for forming a robust predictor applicable to future observational programmes.

As methodology, Spearman's rank correlation coefficient (r_s) is employed. Unlike Pearson, this non-parametric test measures the strength of any monotonic relationship without assuming linearity, being robust against both outliers and the asymmetric distributions typical of dwarf galaxies (Wall et al. 2012). The coefficient r_s ranges from -1 to $+1$. Values of $+1$ and -1 indicate a perfectly monotonically increasing or decreasing relationship, while $r_s = 0$ indicates the absence of a trend.

The choice of the Spearman estimator over Pearson is justified in this context for three reasons. First, the distributions of galaxy physical properties such as mass or equivalent widths show pronounced asymmetric tails even on a logarithmic scale. Second, the relationship between the auroral line rest equivalent width and stellar continuum parameters is not necessarily linear. Third, and perhaps most importantly, some of the most physically significant objects in the sample, such as I Zw 18, are genuine outliers that should not be discarded, and a rank-based estimator handles these naturally without distorting the result.

Two separate correlation matrices were generated to evaluate how the physical dependencies change depending on whether [OIII]λ4363 is detected or not (Figure 8).

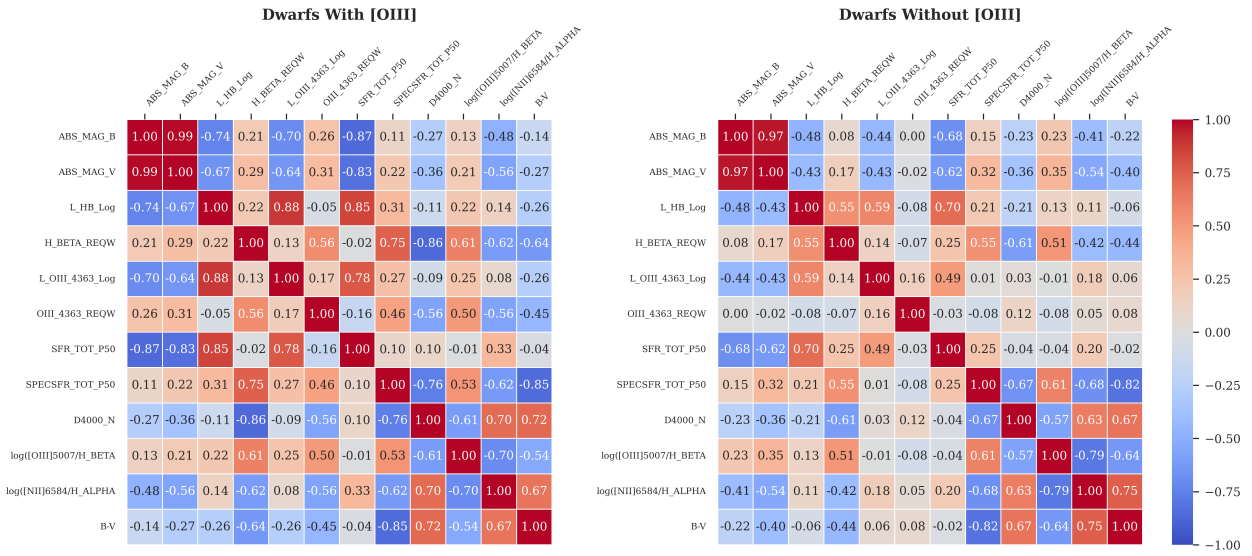

Figure 8: Spearman correlation matrices for photometric and spectral properties. The left panel shows the sub-sample with [OIII]λ4363 detection and the right panel shows the sample without detection.

In the matrix for galaxies with detection, a strong anti-correlation is seen between $EW_0(\mathrm{H}\beta)$ and $D_{4000,N}$ ($r_s \approx -0.86$), with $D_{4000,N}$ and EW_0([OIII]4363) ($r_s \approx -0.56$) having a similar connection. This tells us that a brighter, more evolved stellar continuum tends to reduce or suppress

the detectability of the auroral line, even when the gas itself remains highly excited (Hoyos et al. 2006).

The strongest pattern in the matrix is the tight coupling between starburst-related observables and the auroral line itself. Both $L_{\mathrm{H}\beta}$ and $L_{\mathrm{OIII}\,4363}$ are strongly correlated, as are $L_{\mathrm{OIII}\,4363}$ and the total star formation rate, pointing to auroral-line visibility as something that preferentially occurs in systems undergoing intense recent star formation. This close connection between continuum properties and emission-line strength suggests that the detectability reflects the evolutionary stage of the burst, with $EW_0(\mathrm{H}\beta)$ serving as a natural tracer of burst strength, since large values imply very young stellar populations with high ionising-photon production (Leitherer et al. 1999).

The inclusion of the $D_{4000,N}$ index as a fundamental variable in this analysis is motivated by the work of Cardiel et al. (2003), who identify the 4000 Å discontinuity as a robust indicator for characterising stellar population properties from spectroscopic data. One practical advantage is that it quantifies the continuum level independently of dust extinction, giving a reliable handle on stellar age even in spectra with varying signal-to-noise ratios. Here, its strong anti-correlation with $EW_0(\mathrm{H}\beta)$ and clear link to the specific star formation rate reinforce the picture that galaxies with [OIII]λ4363 detections are dominated by young, compact, and highly active stellar populations.

The matrix for galaxies without [OIII]λ4363 detection tells a different story. The correlations are much weaker and more diffuse. Although some broad trends are still present, the tight coupling between burst strength, continuum age indicators, and auroral-line-related quantities largely dissolves. This suggests that the physical conditions required for detecting [OIII]λ4363 are not common in the non-detected population, with this contrast being one of the main results of the analysis. Galaxies where the auroral line is visible appear to occupy a more extreme and physically coherent regime, defined by low mass, compact structure, high specific star formation rate, and favourable excitation conditions.

In practical terms, this means that [OIII]λ4363 emitters cannot be efficiently selected using a single observable or by applying generic criteria representative of the full dwarf-galaxy population. Their identification requires a combination of the key ingredients revealed by the correlation analysis: strong ongoing star formation, a sufficiently young stellar continuum, and low metallicity. The following section quantifies these dependencies through a systematic sweep of candidate predictors and Bayesian linear regressions, with the aim of identifying which observables provide the most reliable a priori estimate of the auroral-line intensity.

4 Figure of merit for [OIII]λ4363 emitters

To quantify the impact of various parameters on the visibility of the auroral line, a loop of statistics that measure correlations was used, with $\log EW($[OIII]λ4363$)$ as the dependent variable. To ensure the robustness of the results, four different but complementary statistic methods were applied: Pearson's r, Spearman's ρ, distance correlation (dCor) and normalised mutual information (NMI).

Each statistic captures a different type of dependence. Pearson's r measures linear association and serves as the classical reference, Spearman's ρ is non-parametric and robust to asymmetric distributions. If $\rho > r$, it is a sign for the presence of outliers or curvature. The dCor (Székely et al. 2007) detects any form of statistical dependence; in particular, dCor = 0 if and only if the variables are statistically independent. The NMI, computed using the decile discretisation method of Nandi et al. (2024), is insensitive to the geometry of the data space and complements the dCor. If all four statistics converge, then we can say that a real association exists.

The results of this 'sweep' are shown in Table 3, ordered by decreasing $|r|$ in two blocks: direct

spectral indices and variables on a logarithmic scale.

Variable	r	ρ	dCor	NMI	N
Direct measurements					
Lick $H\gamma_A$	-0.708	-0.577	0.672	0.151	1469
Lick $H\beta$	-0.680	-0.538	0.648	0.137	1469
Lick Mg_1	$+0.679$	$+0.551$	0.663	0.144	1469
$\log EW$([Ne III]3869)	$+0.641$	$+0.601$	0.641	0.161	1453
Lick Mg_2	$+0.626$	$+0.501$	0.629	0.129	1469
$\log D_{4000,N}$	-0.613	-0.549	0.621	0.146	1465
$\log EW(\mathrm{H}\beta)$	$+0.455$	$+0.550$	0.545	0.141	1443
Physical radius (kpc)	-0.023	-0.043	0.147	0.026	1469
Derived variables					
$12 + \log(\mathrm{O/H})$	-0.459	-0.485	0.446	0.071	1389
log(sSFR)	$+0.451$	$+0.459$	0.476	0.087	1326
$\log M_\star$	-0.381	-0.367	0.391	0.053	1469
$\log L$([O III]λ4363)	$+0.184$	$+0.185$	0.190	0.036	1469
$\log L(\mathrm{H}\beta)$	-0.036	-0.047	0.088	0.018	1469

Table 3: Correlation sweep between candidate predictors and $\log EW$([O III]λ4363), for the subsample of dwarfs with detection ($M_B > -18$, $S/N > 3$, $N_{\mathrm{total}} = 1469$). All values with $|\rho| > 0.1$ are statistically significant ($p \ll 10^{-3}$); except $\log L(\mathrm{H}\beta)$ and the physical radius (not significant in Pearson and Spearman).

The four statistics are consistent across all variables with $|\rho| > 0.1$, except $\log L(\mathrm{H}\beta)$ and the physical radius, suggesting that most of the associations are real.

The strongest predictors are the four Lick indices, which reach $|r| = 0.63$–0.71 and dCor $= 0.63$–0.67. On one hand, $H\gamma_A$ and $H\beta$ correlate negatively, as expected in our star-forming dwarfs because nebular emission fills in the underlying stellar Balmer absorption and lowers the measured index value. On the other hand, Mg_1 and Mg_2 correlate positively which likely reflects that dwarf galaxies with a detectable λ4363 line often combine a young ionising burst with a pre-existing evolved population that elevates the magnesium indices.

Among the logarithmic variables, $\log EW$([NeIII]3869) is the leading Spearman predictor ($\rho = +0.601$), while $\log D_{4000,N}$ is such in Pearson ($r = -0.613$), reflecting a more linear relationship with [OIII] than the [NeIII] has.

The derived physical quantities (metallicity, stellar mass and sSFR) show moderate correlations ($|r| \approx 0.38$–0.46), and the smaller values for $\log L(\mathrm{H}\beta)$ and the physical radius confirm that the auroral line visibility is controlled by spectral contrast rather than by the total flux or size of the galaxy (Hoyos et al. 2006).

The convergence of all four statistics across the top predictors, and the fact that these are directly observable, motivates their use as predictors in the Bayesian regression of Section 4.2.

4.1 Two Populations: High and Low Ionisation

While plotting these properties against the rest frame [OIII]λ4363 equivalent width, the scatter diagram with $\log EW(\mathrm{H}\beta)$ shows signs visually of bimodality. The point cloud does not follow a continuous, linear distribution but is organised around two areas. To investigate this, we divided the sample at the third quartile of $EW_0(\mathrm{H}\beta)$ of the whole emitters sample ($Q_3 = 45.27$ Å, $\log Q_3 = 1.656$), coinciding with the separation observed in the diagram. The two resulting sub-populations

are going to be referred as the high-ionisation population ($EW_0(\mathrm{H}\beta) > Q_3$, N=365) and the low-ionisation population ($EW_0(\mathrm{H}\beta) \leq Q_3$, N=1108).

The physical interpretation of this is consistent with the bursty nature of star formation in low-mass galaxies (Geha et al. 2012). Below $\log M_\star \approx 8$, the gravitational potential well is shallow enough that the feedback of supernova can expel a large fraction of the gas after a starburst, temporarily suppressing star formation until new gas is accreted. As a result, the sample may be divided into systems caught near the peak of a burst (the high-ionisation population, with a continuum dominated by O and B-type stars) and systems in a later phase, between bursts, where $EW_0(\mathrm{H}\beta)$ has already declined. We applied a Mann-Whitney test that confirms that the high-ionisation population has a significantly lower median stellar mass ($\Delta\tilde{M}_\star < 0$, $p \ll 0.001$), in agreement with this picture.

Table 4 compares the four-statistic correlations with $\log EW_0([\mathrm{OIII}]\,\lambda4363)$ separately for the two ionisation populations, along with the difference Δ between them. It can be seen that $\log EW(\mathrm{H}\beta)$ and $\log D_{4000,N}$ maintain strong associations in both populations, and all four statistics increase uniformly in the high-ionisation regime. However, mass and metallicity show the opposite trend, as their correlations strengthen in the low-ionisation population, which can be due to the fact that at lower $EW_0(\mathrm{H}\beta)$ the metal content and the potential well begin to play a larger role in shaping the auroral-line intensity.

	r			ρ			dCor			NMI		
Predictor	High	Low	Δr	High	Low	$\Delta\rho$	High	Low	ΔdC	High	Low	ΔNMI
Lick Hγ_A	−0.74	−0.41	−0.33	−0.69	−0.27	−0.42	0.74	0.31	+0.43	0.23	0.05	+0.19
Lick Mg$_1$	0.70	0.36	+0.34	0.69	0.24	+0.44	0.70	0.30	+0.40	0.21	0.05	+0.16
Lick Mg$_2$	0.67	0.29	+0.38	0.67	0.19	+0.49	0.68	0.27	+0.41	0.20	0.05	+0.16
log EW([NEIII] 3869)	0.77	0.31	+0.46	0.77	0.31	+0.46	0.76	0.31	+0.45	0.27	0.05	+0.22
Lick Hβ	−0.68	−0.36	−0.33	−0.63	−0.21	−0.42	0.69	0.27	+0.42	0.19	0.04	+0.14
D$_{4000}$	−0.70	−0.19	−0.51	−0.73	−0.23	−0.50	0.74	0.26	+0.49	0.24	0.05	+0.19
log EW(Hβ)	0.69	0.06	+0.64	0.64	0.21	+0.42	0.68	0.21	+0.47	0.19	0.04	+0.15
$\log D_{4000,N}$	−0.76	−0.23	−0.53	−0.73	−0.23	−0.50	0.75	0.26	+0.48	0.24	0.05	+0.19
Physical radius	−0.26	0.13	−0.38	−0.31	0.12	−0.43	0.29	0.18	+0.11	0.07	0.03	+0.05
$12 + \log(\mathrm{O/H})$	−0.58	−0.32	−0.26	−0.55	−0.35	−0.21	0.56	0.33	+0.23	0.17	0.05	+0.13
log(sSFR)	0.36	0.16	+0.19	0.35	0.20	+0.15	0.38	0.21	+0.17	0.12	0.03	+0.08
$\log(M_\star)$	−0.29	−0.16	−0.13	−0.30	−0.16	−0.15	0.30	0.19	+0.11	0.08	0.03	+0.05
$\log L([\mathrm{OIII}]\,4363)$	0.25	0.14	+0.10	0.21	0.17	+0.05	0.22	0.16	+0.06	0.09	0.03	+0.07
$\log L(\mathrm{H}\beta)$	−0.03	−0.10	+0.07	−0.06	−0.10	+0.04	0.12	0.12	−0.01	0.08	0.02	+0.06

Table 4: Comparison of four-statistic correlations with $\log EW([\mathrm{O\,III}]\,\lambda4363)$ by $EW_0(\mathrm{H}\beta)$ population. Δ = High − Low. Populations defined by $\mathrm{Q}_3 = 45.27$ Å.

4.2 Quantifying the Relations: Bayesian Regressions

The univariate scan we did identifies the most relevant predictors, but it does not quantify the slopes of the physical relationships, nor does it account for the measurement uncertainties that affect both the predictor and the response variable. For this purpose, a Bayesian linear regression model was fitted separately for each predictor and each ionisation population, implemented with Stan via `cmdstanpy` with 4 independent chains of 15 000 post-warmup iterations each. Convergence was assessed by requiring $\hat{R} < 1.01$ for all parameters and fewer than five divergent transitions across all chains (Carpenter et al. 2017).

The model we did accounts for the measurement uncertainties in both variables. For a given

predictor x and response $y = \log EW([\mathrm{OIII}]\,\lambda4363)$, the structure is as follows:

$$x_i^{\mathrm{obs}} \sim \mathcal{N}(x_i^{\mathrm{true}},\, \sigma_{x,i}) \tag{1}$$

$$y_i^{\mathrm{obs}} \sim \mathcal{N}(y_i^{\mathrm{true}},\, \sigma_{y,i}) \tag{2}$$

$$y_i^{\mathrm{true}} \sim \mathcal{N}(\beta_0 + \beta_1\, x_i^{\mathrm{true}},\, \sigma_{\mathrm{int}}) \tag{3}$$

where $\sigma_{x,i}$ and $\sigma_{y,i}$ are the individual measurement errors, and σ_{int} is the intrinsic scatter (the physical variability between galaxies not explained by the predictor). We used weakly informative priors $\beta_0, \beta_1 \sim \mathcal{N}(0, 5)$ and $\sigma_{\mathrm{int}} \sim \mathrm{Exp}(1)$ (this last one ensures positivity).

The measurement errors for most of the derived quantities were estimated as $(\mathrm{P}_{84} - \mathrm{P}_{16})/2$, from the catalogue percentile columns, except when the error was directly provided. If the variable was transformed to a logarithmic scale, the error was propagated accordingly.

The Bayesian regressions were fitted for the ten predictors with the most correlation, but for the figures and the summary table we focus on a reduced set of six: $\log D_n(4000)$, $\log EW([\mathrm{NeIII}]\,3869)$, $\log EW(\mathrm{H}\beta)$, $12 + \log(\mathrm{O/H})$, $\log(\mathrm{sSFR})$ and $\log M_\star$. The four Lick indices ($H\gamma_A$, $H\beta$, Mg_1, Mg_2) are excluded from the figures because they are redundant with the spectral indices already included, as $D_n(4000)$ and $\log EW(\mathrm{H}\beta)$ capture the same underlying physics The derived quantities (metallicity, stellar mass and sSFR) are kept because they represent independent physical dimensions of the problem.

Figure 9 shows the regression lines and their predictive bands for the six selected predictors, with the sample split into the high- and low-ionisation populations (red and blue) and the full-sample fit overlaid in green. Several things are immediately visible. For $\log D_n(4000)$ and $\log EW(\mathrm{H}\beta)$ the two populations are clearly separated, with the high-ionisation population showing a steeper slope, especially for $\log EW(\mathrm{H}\beta)$ where the low-ionisation population is nearly flat ($\beta_1 \approx 0.14$) while the high-ionisation one has $\beta_1 \approx 1.32$. For $\log EW([\mathrm{Ne\,III}])$ the separation is also clear but a little less extreme. For the derived quantities the picture is noisier, particularly for $\log(\mathrm{sSFR})$ where the scatter is large, and the two populations overlap considerably. The full-sample fit (green) generally falls between the two population fits, as expected, and in some cases (notably $\log EW(\mathrm{H}\beta)$) it misses the behaviour of both populations, which illustrates why the population split is necessary. In the case of $\log M_\star$, it can be seen that the regressions for both populations run parallel to each other, with the high ionisation population consistently having higher $\log EW([\mathrm{O\,III}]\,\lambda4363)$.

The posterior summaries for all fits are collected in Table 5. In Table 6 we shown an example of the explicit relations. The intrinsic scatter σ_{int} is consistently larger for the derived quantities ($\sim$ 0.18–0.26 dex) than for the directly observed spectral indices ($\sim$ 0.13–0.21 dex), which is consistent with the fact that quantities like stellar mass or metallicity carry additional uncertainties related to the models used that are not fully captured by the measurement error propagation. The slopes β_1 are in all cases significantly different from zero (the HDI 95% intervals do not include zero for the main predictors), confirming that the correlations identified in the univariate sweep translate into well-constrained almost linear relationships. We also did unweighted fits, showing that the difference between the error-weighted and the unweighted fits is generally small for the observed predictors, which suggests that the measurement errors are not large enough to strongly bias the regression in this sample.

A more direct way to quantify the separation between the two populations is to compute how many standard deviations apart the posterior means of β_1 are,

$$\Delta = \frac{|\mu_{\mathrm{high}} - \mu_{\mathrm{low}}|}{\sqrt{\sigma^2_{\mathrm{high}} + \sigma^2_{\mathrm{low}}}}, \tag{4}$$

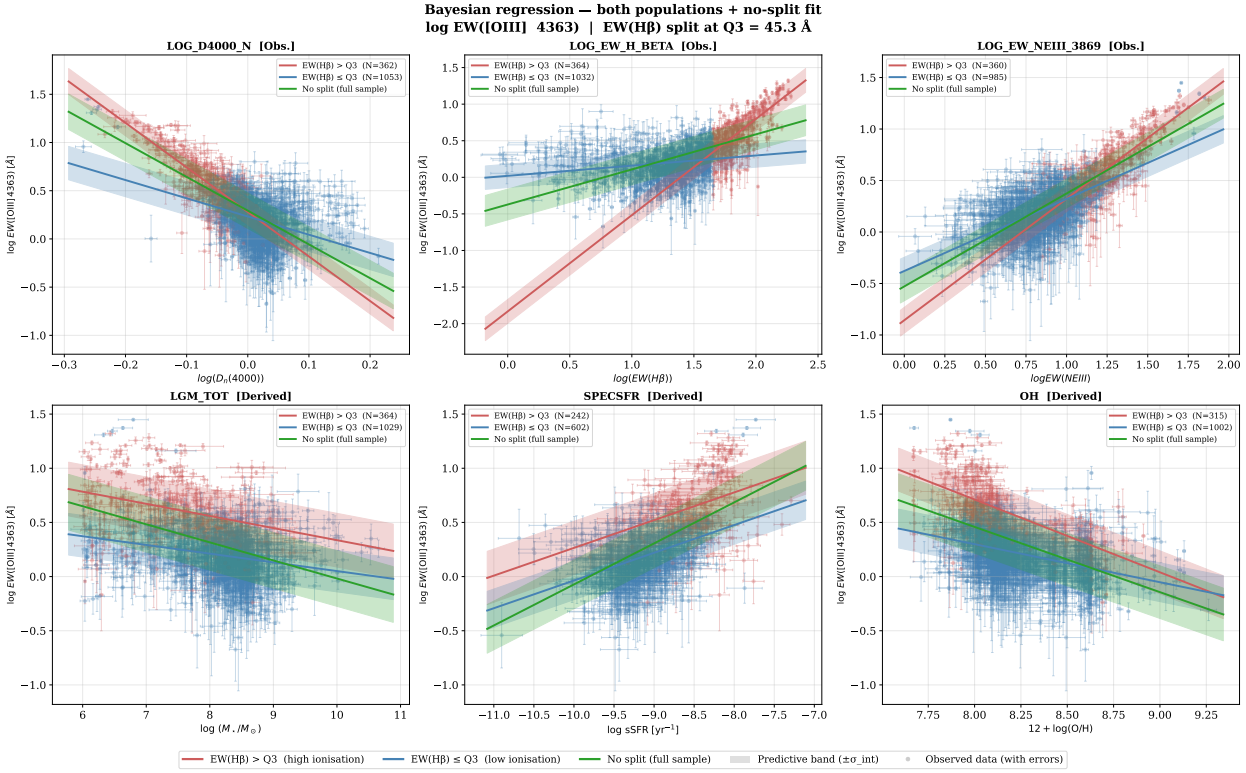

Figure 9: Bayesian linear regressions of $\log EW([\mathrm{O\,III}]\,\lambda4363)$ against six selected predictors. Red lines and points correspond to the high-ionisation population ($EW_0(\mathrm{H}\beta) > Q_3 = 45.3$ Å), blue to the low-ionisation population ($EW_0(\mathrm{H}\beta) \leq Q_3$), and green to the full sample without population split. Shaded bands show the posterior predictive interval ($\pm\sigma_{\mathrm{int}}$). Error bars on individual points represent the measurement uncertainties propagated into the regression.

where σ_{high} and σ_{low} are the posterior standard deviations of β_1 for each population, taken directly from the MCMC chains. The results are as follows: $\log EW(\mathrm{H}\beta)$ shows the largest separation ($\Delta \approx 17\sigma$), followed by $D_n(4000)$ ($\Delta \approx 14\sigma$) and $\log EW_0([\mathrm{Ne\,III}]\,3869)$ ($\Delta \approx 9\sigma$). In contrast, the derived quantities show much weaker or no separation: log(sSFR) gives $\Delta \approx 0\sigma$ (both populations yield $\beta_1 \approx 0.26$), $\log M_\star$ gives $\Delta \approx 1.5\sigma$, and only metallicity reaches a marginally significant value ($\Delta \approx 6\sigma$), consistent with the discussion in Section 4.1.

The differential steepness found for the spectral predictors has a straightforward physical interpretation. In galaxies at the peak of a young burst ($EW_0(\mathrm{H}\beta) > Q_3$), the electron temperature is extremely sensitive to even small changes in continuum age or ionising hardness, because the gas is already close to the maximum collisional excitation of the O^{2+} levels. In the evolved population the electron temperature is lower and the response of the auroral line to changes in the continuum parameters is proportionally more muted, which translates directly into a shallower slope.

The intrinsic scatter σ_{int} also deserves attention. For most of the spectral predictors ($D_n(4000)$, $\log EW([\mathrm{Ne\,III}])$, with $\log EW(\mathrm{H}\beta)$ being a near-exception at 0.162 vs 0.160), σ_{int} is smaller in the high-ionisation population than in the low-ionisation one, indicating that burst-phase galaxies form a physically more homogeneous population whose global properties are tightly regulated by the current starburst. The low-ionisation population, by contrast, is a mixture of galaxies at different post-burst stages, each at a different point in the feedback driven gas replenishment cycle described in Section 4.1, which naturally produces larger galaxy-to-galaxy scatter at fixed predictor value.

Predictor	Population	β_0 [HDI 95%]	β_1 [HDI 95%]	σ [HDI 95%]
$\log \mathrm{EW}(\mathrm{H}\beta)$	$\mathrm{EW} > Q_3$	-1.833 [-2.069, -1.597]	1.316 [1.190, 1.440]	0.162 [0.147, 0.178]
	$\mathrm{EW} \leq Q_3$	0.020 [-0.033, 0.073]	0.139 [0.098, 0.180]	0.160 [0.149, 0.171]
	Full sample	-0.372 [-0.422, -0.322]	0.480 [0.446, 0.513]	0.210 [0.200, 0.221]
	$EW > Q_3$ (unw.)	-1.905 [-2.171, -1.637]	1.338 [1.195, 1.480]	0.208 [0.193, 0.224]
	$EW \leq Q_3$ (unw.)	0.133 [0.088, 0.177]	0.032 [-0.002, 0.068]	0.224 [0.215, 0.234]
$\log D_n(4000)$	$\mathrm{EW} > Q_3$	0.280 [0.246, 0.314]	-4.618 [-4.980, -4.256]	0.134 [0.120, 0.149]
	$\mathrm{EW} \leq Q_3$	0.233 [0.218, 0.247]	-1.890 [-2.176, -1.604]	0.173 [0.162, 0.185]
	Full sample	0.293 [0.283, 0.303]	-3.500 [-3.657, -3.501]	0.184 [0.176, 0.192]
$\log \mathrm{EW}([\mathrm{Ne\,III}]\,3869)$	$\mathrm{EW} > Q_3$	-0.857 [-0.965, -0.747]	1.180 [1.096, 1.263]	0.125 [0.113, 0.139]
	$\mathrm{EW} \leq Q_3$	-0.379 [-0.428, -0.329]	0.700 [0.642, 0.757]	0.133 [0.123, 0.144]
	Full sample	-0.528 [-0.564, -0.492]	0.902 [0.867, 0.938]	0.140 [0.131, 0.149]
$12 + \log(\mathrm{O/H})$	$\mathrm{EW} > Q_3$	6.086 [5.299, 6.863]	-0.672 [-0.768, -0.575]	0.198 [0.180, 0.218]
	$\mathrm{EW} \leq Q_3$	3.110 [2.654, 3.565]	-0.351 [-0.406, -0.296]	0.179 [0.168, 0.191]
	Full sample	5.275 [4.814, 5.735]	-0.602 [-0.658, -0.546]	0.243 [0.232, 0.255]
$\log(\mathrm{sSFR})$	$\mathrm{EW} > Q_3$	2.826 [2.044, 3.608]	0.256 [0.164, 0.349]	0.245 [0.222, 0.272]
	$\mathrm{EW} \leq Q_3$	2.523 [2.102, 2.940]	0.256 [0.210, 0.301]	0.177 [0.162, 0.193]
	Full sample	3.715 [3.421, 4.010]	0.379 [0.346, 0.412]	0.225 [0.212, 0.238]
$\log M_\star$	$\mathrm{EW} > Q_3$	1.455 [1.184, 1.726]	-0.112 [-0.148, -0.076]	0.248 [0.228, 0.270]
	$\mathrm{EW} \leq Q_3$	0.855 [0.685, 1.027]	-0.080 [-0.101, -0.060]	0.192 [0.181, 0.204]
	Full sample	1.650 [1.499, 1.802]	-0.167 [-0.186, -0.148]	0.257 [0.246, 0.269]

Table 5: Posterior summaries of the Bayesian linear regressions of $\log \mathrm{EW}([\mathrm{O\,III}]\,\lambda4363)$ against each physical predictor. Upright rows correspond to the error-weighted model (including intrinsic scatter σ_{int}); *italic rows* display the unweighted model. Unweighted runs are explicitly shown only for the first predictor as a representative baseline to save space, since the remaining fits show minimal, non-significant discrepancies from their error-weighted counterparts. Values represent posterior means with 95% HDI in brackets.

Predictor (x)	Explicit Analytical Fit ($y = \beta_0 + \beta_1 x$)
$\log \mathrm{EW}(\mathrm{H}\beta)$	$\log \mathrm{EW}([\mathrm{O\,III}]\,\lambda4363) = -1.833 + 1.316 \times \log \mathrm{EW}(\mathrm{H}\beta)$
$\log D_n(4000)$	$\log \mathrm{EW}([\mathrm{O\,III}]\,\lambda4363) = 0.280 - 4.618 \times \log D_n(4000)$
$\log \mathrm{EW}([\mathrm{Ne\,III}]\,3869)$	$\log \mathrm{EW}([\mathrm{O\,III}]\,\lambda4363) = -0.857 + 1.180 \times \log \mathrm{EW}([\mathrm{Ne\,III}]\,3869)$

Table 6: Explicit linear expressions derived for the high-ionisation population ($EW_0(\mathrm{H}\beta) > Q_3$) using the posterior mean estimates of the intercept (β_0) and slope (β_1).

5 The case of HeIIλ4686

While OIII allows us to derive metallicity estimates and electron temperature, HeIIλ4686 permits us understand the nature and hardness of the ionising radiation field. With an ionisation potential of 54.4 eV, roughly twice that of hydrogen, nebular recombination emission requires an extraordinarily hard radiation field. In the context of this study (star-forming dwarf galaxies), the detection of HeIIλ4686 nebular emission is a tracer of either the presence of Wolf-Rayet stars, high-mass X-ray binaries (HMXB) or post-AGB stars (Kehrig et al. 2018).

The HeIIλ4686 line was not accessible through the MPA-JHU catalogue. For that reason, we searched for someone's work that included SDSS galaxies and this particular line. We found (Shirazi et al. 2012)'s catalogue in Vizier, in which the HeIIλ4686 line was obtained with a pipeline detailed in (Brinchmann et al. 2008) which allowed for it to be cross-matched with our sample of dwarf galaxies, yielding only the star-forming and HeII-emitting galaxies, in the form of a subsample

with reliable log(HeII/Hβ) ratios. However this sample is very small, of only 33 galaxies, so the statistical uncertainties are large, and the results should be interpreted as preliminary. It should be noted that the equivalent widths were not available, and we will be using the flux ratios as proxy.

The same statistics were used to analyse if any correlation is present between log(HeII/Hβ) and the properties used before. The results are shown in Table 7.

Variable	r_P	ρ_s	dCor	NMI	N
log EW(Hβ)	-0.563	-0.597	0.598	0.580	31
log D4000_N	+0.512	+0.573	0.553	0.503	33
Physical radius (kpc)	-0.014	-0.160	0.245	0.503	33
log EW([NEIII]3869)	-0.595	-0.637	0.604	0.540	33
log EW([OIII]4363)	-0.439	-0.430	0.451	0.540	33
Lick Hγ_A	+0.452	+0.592	0.546	0.521	33
Lick Mg1	-0.574	-0.682	0.634	0.595	33
Lick Mg2	-0.585	-0.636	0.616	0.540	33
Lick Hβ	+0.430	+0.554	0.527	0.558	33
log O/H	+0.106	-0.112	0.293	0.562	32
log(sSFR)	-0.326	-0.368	0.412	0.541	31
log(M$\star$)	-0.173	-0.266	0.340	0.540	33
log L([OIII]4363)	-0.515	-0.540	0.562	0.540	33
log L(Hβ)	-0.504	-0.540	0.570	0.558	33

Table 7: Statistical correlations of galaxies with log(HeII/Hβ).

Figure 10 shows the Bayesian regressions of log(He II/Hβ) on the same six selected predictors as before with λ4363 emitters. A fixed uncertainty of 0.1 dex was assumed for all objects as individual flux errors were not reported for the ratio. It is a conservative but realistic estimate for a weak line at the typical SNR of the sample, small enough not to dominate the intrinsic scatter, large enough to acknowledge that HeII is noisier than stronger lines like Hβ.

Predictor	β_0	β_1	σ
D4000_N	-2.801 [-3.368, -2.221]	+1.202 [+0.486, +1.901]	0.209 [0.152, 0.284]
LOG_EW_H_BETA	-0.841 [-1.378, -0.297]	-0.537 [-0.830, -0.253]	0.215 [0.153, 0.291]
LOG_EW_NEIII_3869	-1.230 [-1.544, -0.919]	-0.477 [-0.711, -0.234]	0.198 [0.141, 0.270]
LGM_TOT	-1.321 [-2.388, -0.257]	-0.073 [-0.222, +0.080]	0.255 [0.189, 0.345]
SPECSFR	-3.933 [-6.284, -1.412]	-0.249 [-0.533, +0.049]	0.233 [0.166, 0.321]
OH	-2.438 [-4.615, -0.305]	+0.077 [-0.186, +0.347]	0.235 [0.172, 0.315]

Table 8: Bayesian regression summary (Response: log(HeII/Hβ))

One of the strongest predictors of log(HeII/Hβ) is $D4000_N$, which shows a significant positive slope. This suggests that HeII emission is more prominent in galaxies with a significant evolved stellar component (post-AGB stars) or in the post-burst phase when Wolf-Rayet stars and HMXBs dominate the ionising spectrum, while the continuum is dominated by longer-lived stars. Or potentially Population III stars in extreme cases as recently confirmed by JWST observations near GN-z11 (Rusta et al. 2026; Übler et al. 2026). By contrast, log EW(Hβ) and log EW([NeIII]3869) show significant negative slopes, indicating that stronger current star formation is associated with lower HeII/Hβ.

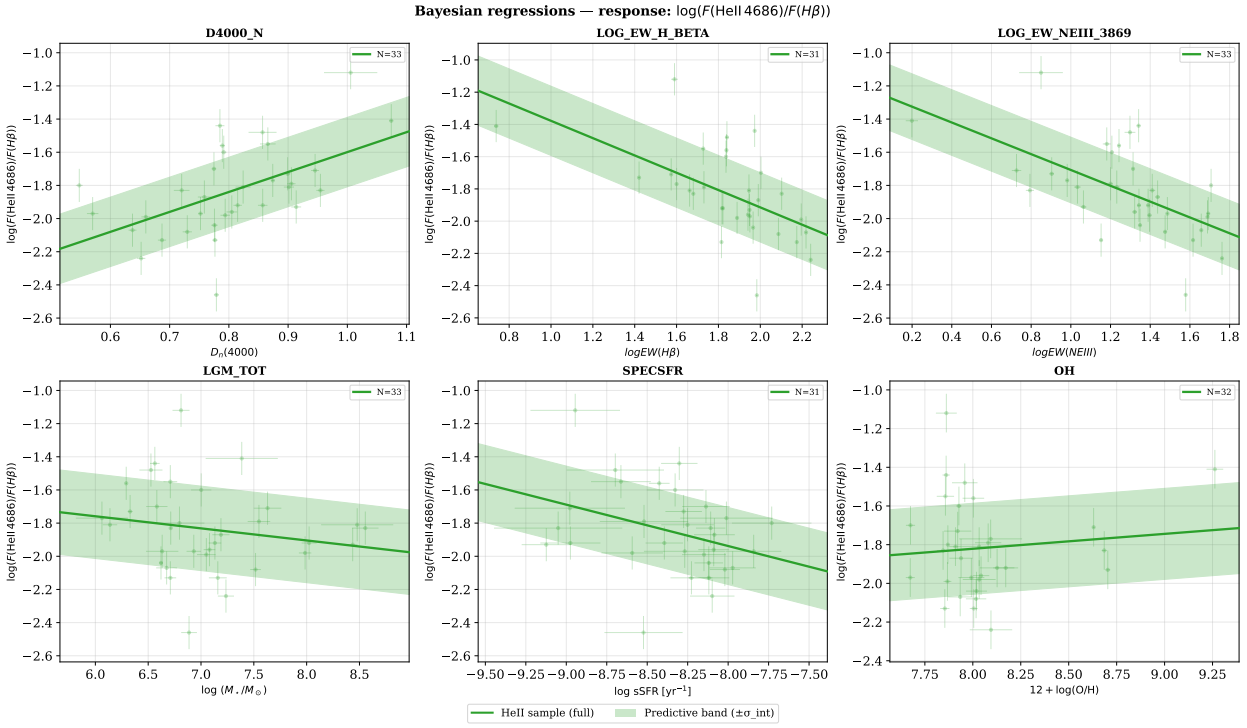

Figure 10: Bayesian linear regressions of log(He II/Hβ) on three selected observed predictors and three derived predictors. The coloured band shows the predictive interval: both the uncertainty of the fitted parameters and the intrinsic scatter of the data.

6 λ4363 emitters at different redshifts: A scientific case for the MOSAIC instrument at ELT

The Exposure Time Calculator (ETC) for the MOSAIC instrument at the future Extremely Large Telescope (ELT) was provided by the MOSAIC team at UCM (Puech et al., private communication). This tool has two formats: an excel file and a python version (Delgado 2027). A survey of OIIIλ4363 emitters at $z > 0.5$ would provide a sample of low-metallicity dwarfs over a lookback time of $\sim$5–8 Gyr, enabling the study of their evolution across time.

With the exposure time per integration fixed at DIT = 1200 s, we varied the number of integrations (NDIT) to determine the total observing time required to detect [OIII]λ4363 in our dwarf-galaxy sample at different redshifts. To do so, we did the reverse process that we used at the start of this study. As the ETC takes the apparent magnitude in the Sloan bands, the absolute magnitudes in the B band had to be transformed (via the Lupton equations where we fixed the colour of the galaxy with the median of our emitters sample: $g - r = 0.20$) and then all the corrections reversed (K-correction, and distance modulus) to get an apparent final magnitude to introduce in the ETC. It should be noted that the extinction correction was not used, as it depends on where the galaxy is located and therefore the following analysis is approximate.

At the same time the redshift couldn't be chosen at random. Due to the OH emission lines from the Earth's upper atmosphere present in the sky, the OIIIλ4363 and Hβ lines have to fall in the few clean windows available. For that we used the spectrum derived for Cerro Paranal in (Rousselot et al. 2000), only a few kilometres away from the future ELT, and derived which redshifts would have those specific lines available in the galaxies' spectrum.

The value established for a usable detection is that the SNR of the continuum has to be at least 3. This is a minimum threshold that ensures the continuum is detected, though higher SNR would be preferred for precise measurements of the auroral line.

z	Obs. λ_{OIII}	Obs. $\lambda_{H\beta}$	M_B	m	NDIT	Time [h]
0.500	6544	7292	-15	26.75	80	26.7
0.525	6654	7413	-16	26.73	50	16.7
0.550	6763	7535	-16	26.89	80	26.7
0.650	7199	8021	-17	26.48	30	10.0
0.675	7308	8142	-17	26.62	50	16.7
0.700	7417	8264	-17	26.75	50	16.7
0.875	8181	9114	-18	26.62	50	16.7
0.970	8595	9576	-18	27.04	120	40.0

Table 9: Predicted observing times for [OIII]λ4363 detection with MOSAIC/ELT at different redshifts. Columns: redshift (z), observed wavelengths for [OIII] and Hβ, limit absolute B magnitude, apparent magnitude, number of integrations (NDIT), total observing time. Criteria: $\mathrm{SNR}_{\mathrm{cont}} \geq 3$, colour fixed at $(\mathrm{g} - \mathrm{r}) = 0.20$ (median of emitters sample).

If the goal is to carry out a survey of active star-forming galaxies with [OIII]λ4363 detections, which enables the use of the direct-method calculation of the gas-phase abundance, the results in Table 9 show the necessary observing time for different redshifts for an individual galaxy.

7 Summary and Conclusions

This work has characterised the physical properties of star-forming dwarf galaxies in the low-redshift universe through the lens of the auroral line [OIII]λ4363, using spectroscopic and photometric data from SDSS DR8. The main results and conclusions are the following.

1. The primary result of this work is the identification of directly observable and easily derived physical parameters that provide a reliable a priori estimate of the presence and intensity of the auroral line [OIII]λ4363. The strongest individual predictors of $\log EW_0$([OIII]λ4363) are $\log EW_0$(Hβ) ($\rho = +0.550$) and the $D_{4000,N}$ break index ($r = -0.613$, $\rho = -0.549$), both of which are accessible from low-resolution spectroscopy across a broad redshift range. The $\log EW_0$([NeIII]λ3869) is the leading Spearman predictor among logarithmic variables ($\rho = +0.601$). The convergence of four independent statistics (Pearson r, Spearman ρ, dCor and NMI) across all top-ranked predictors confirms that these associations are robust and not an artefact of the choice of method. These results are of direct scientific relevance for the design of future observational programmes with instruments such as MOSAIC at the ELT.

2. Dwarf galaxies with [OIII]λ4363 detection are systematically lower in stellar mass ($\log M_\star \sim$ 8.2 vs. 8.9), bluer in colour ($g-r \sim 0.20$ vs. 0.43 mag), more compact ($R_{50} \sim 1.6$ vs. 3.3 kpc), younger ($D_{4000,N} \sim 1.01$ vs. 1.21) and more intensely star-forming ($\log$ sSFR ~ -9.05 vs. -9.78) than dwarf galaxies of comparable luminosity without auroral-line detection. This is consistent with the results of Hoyos et al. (2006) for HII-galaxy samples in the Local Universe, and reflects the fact that the visibility of the auroral line is controlled by spectral contrast rather than by total flux or galaxy size.

3. The BPT diagram confirms that almost all [OIII]λ4363 emitters are powered by pure star formation, and are concentrated at the low-metallicity, high-excitation extreme of the star-

forming sequence. This location is directly analogous to that occupied by high-redshift galaxies with direct-method metallicities measured by JWST (Laseter et al. 2024), validating the use of this low-redshift sample as a reference population for the design of intermediate- and high-redshift programmes.

4. There is a statistically significant morphological segregation ($\chi^2 = 87.09$, $p \ll 0.001$): dwarf galaxies with [OIII]λ4363 are preferentially compact or irregular systems in a starburst phase above the star-forming main sequence. This is consistent with the interpretation that they are low-redshift analogues of the faint, bursty dwarf galaxies responsible for the reionisation of the universe (Atek et al. 2024; Laseter et al. 2024).

5. The sample of [OIII]λ4363 emitters divides naturally into two ionisation populations, separated at the third quartile of $EW_0(\mathrm{H}\beta)$ ($Q_3 = 45.3$ Å). Bayesian linear regressions with measurement errors in both axes confirm that all spectral predictors are significantly steeper in the high-ionisation population, with non-overlapping 95% HDI intervals: $\Delta \approx 17\sigma$ for $\log EW(\mathrm{H}\beta)$ and $\Delta \approx 14\sigma$ for $\log D_{4000,N}$. This bimodality is physically interpreted as the contrast between galaxies caught at the peak of a starburst and systems in a later, post-burst phase, in line with the bursty nature of star formation in low-mass galaxies (Atek et al. 2022).

6. A galaxy is a strong candidate for detectable [OIII]λ4363 emission, and therefore accessible to direct-method gas-phase abundance determination, when it satisfies one or more of this properties: $D_{4000,N} \lesssim 1.1$, $EW_0(\mathrm{H}\beta) \gtrsim 15$ Å, $\log EW_0([\mathrm{NeIII}]\lambda3869) \gtrsim 1$, and compact morphology with blue colour ($g-r \lesssim 0.30$ mag). These criteria are directly applicable to photometric and low-resolution spectroscopic catalogues at different redshifts without requiring prior knowledge of the auroral line itself.

7. The ETC analysis for the MOSAIC instrument at the ELT demonstrates that a survey of [OIII]λ4363 emitters at $0.5 \lesssim z \lesssim 0.97$ is observationally feasible within atmospheric emission windows, but is limited to galaxies brighter than $M_B \approx -15$ to -18 (depending on redshift), requiring between $\sim$10 and $\sim$40 hours of integration per object. Only the most luminous end of the low-redshift dwarf population studied here will therefore be reachable at intermediate redshifts, making the pre-selection criteria derived in this work essential for an efficient use of telescope time.

8. The results of this work will lay the scientific groundwork for the JAEN-DEEP project (Joint Analysis of Epochal Near-and-distant Dwarf Extragalactic Emission Properties), a multi-epoch observational programme aimed at characterising the emission properties of star-forming dwarf galaxies across cosmic time, from the local universe out to the epoch of reionisation. The selection criteria and observational predictors derived here will serve as the primary reference for designing and optimising future spectroscopic surveys with MOSAIC at the ELT.

A sample of 25 galaxies from this study, that will be the core of JAEN-DEEP are (all start with SDSS, they may have more common names): J121402.47+534517.3, J115441.22+463636.3, J122358.19+072701.7, J093402.38+551423.1, J112504.00+280935.6, J122025.78+331431.7, J114506.26 +501802.4, J112800.19+250411.5, J100054.76+251352.8, J122712.80+073820.5, J094718.35 +413816.4, J094254.27+340411.9, J113623.82+470929.1, J171236.63+321633.4, J084236.57+103313.9, J133126.91 +415148.2, J132723.28+402204.1, J013352.55+134209.5, J153155.70+141915.7, J132852.95 +155934.3, J113116.36+570358.8, J101227.02+122037.4, J100348.66+450457.6, J231903.23+010853.4, J025234.29 +011443.9.

This sample represents the extreme emission line systems. We tested some of our empirical expressions to predict the $\log EW_0([\text{OIII}]\lambda 4363)$ in this sample and compared them to the observed value, finding mean absolute errors of ~ 0.15 dex.

This study was realised with the help of the IPARCOS prize for master's thesis. The code used can be accesed through Github:
`https://github.com/lauramedinacrespo/star-forming-dwarfs-from-SDSS`.

8 References

Abazajian et al. (2004). *AJ* 128.1, pp. 502–512.

Aihara et al. (2011). *ApJS* 193.2, p. 29.

Anderson et al. (1952). *The Annals of Mathematical Statistics* 23.2, pp. 193–212.

Andrews et al. (2013). *ApJ* 765, p. 140.

Atek et al. (2022). *MNRAS* 511.3, pp. 4464–4479.

Atek et al. (2024). *Nature* 626.8001, pp. 975–978.

Baldwin et al. (1981). *PASP* 93, pp. 5–19.

Balogh et al. (1999). *ApJ* 527.1, pp. 54–79.

Brazzini et al. (2024). *A&A* 691, A173.

Brinchmann et al. (2004). *MNRAS* 351.3, pp. 1151–1179.

Brinchmann et al. (2008). *A&A* 485.3, pp. 657–677.

Bruzual et al. (2003). *MNRAS* 344.4, pp. 1000–1028.

Cardamone et al. (2009). *MNRAS* 399.3, pp. 1191–1205.

Cardiel et al. (2003). *A&A* 409, pp. 511–522.

Carpenter et al. (2017). *Journal of Statistical Software* 76.1, pp. 1–32.

Chilingarian et al. (2010). *MNRAS* 405.3, pp. 1409–1420.

Cook et al. (2014). *MNRAS* 445.1, pp. 890–898.

Delgado (2027). PhD thesis, (UCM), in prep.

Gburek et al. (2019). *ApJ* 887.2, p. 168.

Geha et al. (2012). *ApJ* 757.1, 85, p. 85.

Grebel (1998). *Highlights of Astronomy* 11A, p. 125.

Hoyos et al. (2006). *MNRAS* 365.2, pp. 454–468.

Kauffmann et al. (2003). *MNRAS* 341.1, pp. 33–53.

Kehrig et al. (2016). *MNRAS* 459.3, pp. 2992–3004.

Kehrig et al. (2018). *MNRAS* 480.1, pp. 1081–1095.

Kennicutt et al. (2012). *ARA&A* 50.1, pp. 531–608.

Kewley et al. (2001). *ApJ* 556, pp. 121–140.

Kewley et al. (2005). *PASP* 117.829, pp. 227–244.

Kewley et al. (2019). *ARA&A* 57.1, pp. 511–570.

Kolmogorov (1933). *Giornale dell'Istituto Italiano degli Attuari* 4, pp. 83–91.

Laseter et al. (2024). *A&A* 681, A70.

Leitherer et al. (1999). *ApJS* 123, pp. 3–40.

Llerena, M. et al. (2026). *A&A* 708, A152.

Lupton (2005). `https://www.sdss3.org/dr8/algorithms/sdssUBVRITransform.php`.

Lupton et al. (2001). *ASP Conf. Ser.* 238, p. 269.

Mazzolari et al. (2024). *A&A* 691, A345.

Nandi et al. (2024). *JCAP* 2024.02, p. 012.

Osterbrock et al. (2006). 2nd ed. University Science Books.

Rousselot et al. (2000). *A&A* 354, pp. 1134–1150.

Rusta et al. (2026). prepint.

Sanders et al. (2016). *ApJL* 825.2, p. L23.

Schlegel et al. (1998). *ApJ* 500.2, pp. 525–553.

SDSS-III Collaboration (2012). SDSS-III Data Release 8. URL: `https://www.sdss3.org/dr10/spectro/galaxy_mpajhu.php`.

Shirazi et al. (2012). *MNRAS* 421.2, pp. 1043–1063.

Smirnov (1948). *The Annals of Mathematical Statistics* 19.2, pp. 279–281.

Strauss et al. (2002). *AJ* 124.3, pp. 1810–1824.

Székely et al. (2007). *The Annals of Statistics* 35.6, pp. 2769–2794.

Tremonti et al. (2004). *ApJ* 613.2, pp. 898–913.

Übler et al. (2026). prepint.

Wall et al. (2012). 2nd. 8. Cambridge University Press.

Willett et al. (2013). *MNRAS* 435, pp. 2835–2860.